Frontiers in Heat and Mass Transfer

Tech Science Press

https://doi.org/10.32604/fhmt.2026.079520

ARTICLE

Numerical Investigation on Flow Characteristics of Non-Newtonian Fluids in Microchannels with Microcavities

Yi Huang[1], Ran Gao[1], Hao Ye[1], Weidong Fang[1], Xiaopeng Shang[2] and Haiwang Li[1,*]

[1]National Key Laboratory of Science and Technology on Aero-Engine Aero-Thermodynamics, Research Institute of Aero-Engine, Beihang University, Beijing, China

[2]School of Mechanical Engineering and Automation, Beihang University, Beijing, China

*Corresponding Author: Haiwang Li. Email: lihaiwang@buaa.edu.cn

Received: 22 January 2026; Accepted: 12 March 2026; Published: 29 June 2026

ABSTRACT: Efficient transport of non-Newtonian fluids plays an important role in energy and thermal management systems. However, drag reduction characteristics and fluid behavior of non-Newtonian fluids in microchannels with structures are still under investigated, which is essential for lowering pumping power, improving transport and heat transfer efficiency to optimize microfluidic device design. This study systematically investigates the drag reduction performance of non-Newtonian fluids in microchannels with various cavities through numerical simulations and experimental verification. The effects of cavity incidence angle, structural smoothness, non-Newtonian rheological parameters, and shape parameters are analyzed. The drag reduction efficiencies under both cavities and non-Newtonian fluids conditions were tested, and found to increase by up to 7.6% at low flow rates, but decrease at higher flow rates. Among all the configurations, isosceles triangular and semicircular cavities exhibit superior drag reduction. Non-Newtonian parameters, the consistency coefficient m and power law index n, both present nonlinear behavior with the pressure drop rate. Geometric parameters, shape ratio, depth ratio, and spacing ratio have little effect on the drag reduction effect. Therefore, our work clarifies the coupling mechanisms of drag reduction between fluid rheology and micro cavities, which provides beneficial guidance for the design of the micro channel for optimizing the transport performances of non-Newtonian fluids.

KEYWORDS: Non-Newtonian fluid; drag reduction; microchannel; microcavities

1 Introduction

Fluid flow within microchannels has gained significant attention in recent years due to its essential applications in microfluidic systems [1–3], lab-on-chip devices [4,5], and heat transfer enhancement [6,7]. In conventional fluid dynamics, the Newtonian fluid flow is well-understood, governed by established models such as the Darcy–Weisbach equation [8]. However, many fluids encountered in real-world applications do not exhibit the simple linear relationship between shear stress and shear rate characteristic of Newtonian fluids. Instead, they exhibit complex behaviors that are influenced by factors such as shear rate, viscosity, and elasticity, making them non-Newtonian fluids. These fluids include polymers [9], slurries [10], blood [11], and suspensions [12], which exhibits complex flow behavior that significantly differs from that of Newtonian fluids due to their shear-dependent viscosity [13]. The unique behavior presents both challenges and opportunities for enhancing the performance of microfluidic devices in a wide array of fields, including chemical analysis [14], biomedical diagnostics [15], and energy systems [16].

Research into the non-Newtonian fluids in microchannels has garnered considerable attention in recent years [17]. The flow behavior of non-Newtonian fluids is found to be influenced by a range of factors such as shear thinning, shear thickening, and viscoelastic effects [18]. Chen et al. [19] investigated the flow behavior of non-Newtonian fluids by analyzing velocity profiles in mini-channels. The power-law index derived from velocity measurements across different Reynolds numbers showed good agreement with rheometer data, validating the feasibility of using velocity profile analysis as an alternative method for rheological characterization. Fischer et al. [20] investigated the effects of non-Newtonian rheology on flow and mass transfer in spacer-filled channels using the power-law model, with index of 0.7, 1.0, and 1.3 representing shear-thinning, Newtonian, and shear-thickening behaviors, respectively. The results showed that shear-thinning fluids yielded the lowest pressure drop, leading to the highest spacer efficiency in all configurations. Tang et al. [21] experimentally compared the flow behavior of deionized water and polyacrylamide (PAM) solution in microchannels. The friction factors of the shear-thinning PAM solution significantly exceeded those predicted by conventional theoretical models. Dong and Liu [22] conducted a multi-objective optimization study on heat transfer in microchannels for non-Newtonian fluids. The results revealed that structural differences between optimal designs for non-Newtonian and Newtonian fluids become more pronounced at low Reynolds numbers. Under the same conditions, blood (non-Newtonian fluid) exhibited higher energy dissipation but also superior heat transfer performance compared to water (Newtonian fluid).

Microstructures such as ribs [23], cavities [24], and pillar arrays [25] to generate secondary flows, are commonly introduced in microchannels to generate secondary flows, promote mixing, and enhance transport efficiency. Li et al. [26] investigated the flow structure and heat transfer behavior of non-Newtonian fluids in microchannel heat sinks incorporating dimples and protrusions. Their results demonstrated that heat transfer performance was significantly improved, with notable coupling effects observed between fluid concentration, flow rate, and the geometric parameters of micro structures. Raihan et al. [27] studied non-Newtonian fluid flow in single-cavity microchannels. The flow inertia governs vortex generation in expansion zones, whereas shear-thinning behavior facilitates flow separation near contractions. The combined effects of inertia and shear-thinning are strongly modulated by the degree of confinement. Farahani et al. [28] numerically investigated the heat transfer performance of non-Newtonian fluid flow in a ribbed microchannel subjected to pulsating impingement jets. In the single-jet mode, the heat transfer was found to be highly dependent on the jet injection angle. The four-jet mode with a 90° spray angle delivered the best thermal performance, outperforming both the single- and two-jet modes. While some studies have explored the flow and thermal behavior of non-Newtonian fluids in structured microchannels, most of them focus on specific fluid types or single geometric configuration. The coupled effects between non-Newtonian fluid properties and geometric parameters remains insufficiently understood. To bridge this gap, a systematic framework is needed to reveal their interaction for formulating generalizable design strategies in microfluidic applications.

This work evaluates the flow performance of non-Newtonian fluids inside a micro-channel with different cavities through combination of numerical simulation and experiment methods. The details of velocity and pressure distributions inside the micro-channel are obtained from numerical simulation results which are then verified using corresponding measurements from the experimental results. In addition, a sequential exploration of flow behavior modification effects resulting from changes in the incident angle of cavity, structural smoothness, as well as the non-Newtonian rheological parameter and shape parameters like aspect ratio, depth ratio, and spacing ratio is performed. Based on the combined use of above analyses, this paper reveals the drag reduction effect developed due to non-Newtonian rheology acting together with microcavity-induced flow disturbance, making the mechanism of coupled phenomena a systematized explanation. Moreover, it also provides help about the design of better geometrical arrangements of microchannels aimed at increasing non-Newtonian fluid transportation efficiency for energy or heat management application.

2 Numerical and Experimental Method

2.1 Computation Model

Two groups of wall-cavity structures are designed in this work, as illustrated in Fig. 1. The baseline channel has W = 0.3 mm and H = 0.2 mm, giving $D_h = 2WH/(W+H)$ = 0.24 mm = 240 μm. The straight microchannel (No. 1) is adopted as the reference case. The first group employs the incidence angle as the primary design variable, represented by the right triangle (No. 2), isosceles triangle (No. 3), and left triangle (No. 4). The second group focuses on the structural smoothness, including the rectangle (No. 5), trapezoid (No. 6), and semicircle (No. 7). In all cases, the cavity depth (H_c) is fixed at 0.1 mm, with the cavity width (L_c) along the flow direction set to 0.2 mm and the spacing (S) maintained at 0.6 mm. The channel width W, height H and length L are set as 0.3, 0.2 and 40 mm, respectively. The volumetric flow rate is varied from 500 to 300,000 μL/h, representing a broad spectrum of microfluidic applications.

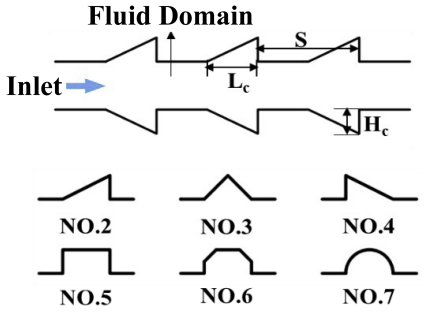

Figure 1: Array cavity structures.

Navier-Stokes equations for a non-Newtonian fluid in the steady state are given as follows:

Continuous equation:

$$\frac{\partial}{\partial x_i}(\rho u_i) = 0 \tag{1}$$

Momentum equation:

$$\frac{\partial}{\partial x_i}\left(\rho u_i u_j\right) = -\frac{\partial p}{\partial x_j} + \frac{\partial}{\partial x_i}\left[\mu\left(\frac{\partial u_j}{\partial x_i} + \frac{\partial u_i}{\partial x_j}\right)\right] \tag{2}$$

where ρ is the density, u is the velocity of the fluid, μ is the dynamic viscosity, and x, y, z represent the X, Y, Z direction in the coordinate system, respectively. For Newtonian fluids, μ can be treated as a constant value. For non-Newtonian fluids with complex rheological properties, μ depends on the shearing rate during the fluid flow. A two-parameter power-law (Ostwald–de Waele) model characterizes non-Newtonian fluid behavior by relating the apparent viscosity to the local shear rate as follows [29]:

$$\mu = m\left(\dot{\gamma}_{yx}\right)^{n-1} = m\left|\frac{\partial u_x}{\partial y} + \frac{\partial u_y}{\partial x}\right|^{n-1} \tag{3}$$

where m is the consistency coefficient and n is the power law index. This formulation captures shear-thinning behavior ($n < 1$), Newtonian behavior ($n = 1$), and shear-thickening behavior ($n > 1$), providing a simple yet effective framework for modeling complex fluids across diverse engineering and energy applications.

Although the governing equations are solved in dimensional form, dimensionless variables are introduced in post-processing for generalization and comparison. Using $L_s = D_h$ and $U = u_{\text{ave}}$, we define $x^* = x/D_h$, $\mathbf{u}^* = \mathbf{u}/u_{\text{ave}}$, and $p^* = (p - p_{\text{out}}) / \left(\rho u_{\text{ave}}^2\right)$.

In this numerical simulation, boundary conditions are set as follows:

Inlet:

$$u = u_{\text{in}}, x = 0 \tag{4}$$

Outlet:

$$P_{out} = 0\ \text{Pa}, x = L \tag{5}$$

Subscripts "in" and "out" refer to the inlet and outlet, respectively. All remaining walls are modeled with no-slip boundary conditions.

2.2 Data Reduction

Dimensionless parameters such as Reynolds number (*Re*), friction factor (f), Poiseuille number (*Po*), are calculated as follows.

Reynolds number is given by [21]

$$Re = \frac{\rho u_{\text{ave}}^{2-n} {D_{\text{h}}}^n}{m} \left(\frac{n}{a + bn}\right)^n \cdot 8^{1-n} \tag{6}$$

where u_{ave} is the average velocity, D_{h} is the hydraulic diameter of the microchannel, a and b are rectangular-duct geometry factors and for $W/H = 1.5$ as 0.2234 and 0.6947, respectively [21].

The strain-rate tensor is

$$\mathbf{D} = \left(\nabla \mathbf{u} + (\nabla \mathbf{u})^T\right)/2 \tag{7}$$

the shear-rate magnitude is

$$|\dot{\gamma}| = \sqrt{2\mathbf{D}{:}\,\mathbf{D}} \tag{8}$$

In the power-law model

$$\mu = m\,|\dot{\gamma}|^{n-1} \tag{9}$$

where m is the consistency index (units: Pa s^n) and n is the flow behavior index ($n < 1$ shear-thinning; $n = 1$ Newtonian).

The deviatoric stress is

$$\boldsymbol{\tau} = 2\mu\mathbf{D} \tag{10}$$

The Poiseuille number (*Po*) is defined as

$$\begin{cases} Po = f \cdot Re \\ f = \dfrac{2\Delta P D_h}{\rho u^2 L} \end{cases} \tag{11}$$

where ΔP is the pressure drop between the inlet and outlet of the microchannel. We use FLUENT 19.0 with a pressure-based solver to compute the governing equations. The SIMPLE algorithm and a second-order upwind discretization scheme are applied. The convergence is reached when the residuals of the energy, continuity, and momentum equations dropped below 10^{-7}.

2.3 Mesh Independence

Prior to performing detailed simulations, a mesh-independence study is conducted for the straight channel. The test condition is set at a flow rate of 1.67 mL/min with a non-Newtonian fluid characterized by m = 0.032 and n = 0.79. Six grid systems are generated, ranging from 70,000 to 6,300,000 cells. The relative error of key physical quantities, including f and Po, is evaluated using Eq. (9):

$$e\% = \left| \frac{J_2 - J_1}{J_1} \right| \times 100\% \tag{12}$$

where J_1 denotes the value calculated with the finest grid (6,300,000 cells), and J_2 represents the corresponding value obtained from a coarser grid. As shown in Table 1, the fourth mesh level achieves a good compromise between computational accuracy and efficiency; thus, it is adopted for subsequent structured channel simulations.

Table 1: Mesh independence of the straight microchannel.

No.	Grid Numbers ($\times 10^5$)	ΔP (kPa)	*e%*
1	0.7	40.10	4.75
2	1.3	40.87	2.92
3	2.4	41.28	1.95
4	17.0	41.98	0.27
5	35.5	41.99	0.26
6	63.0	42.10	–

Given that wall-structured microchannels exhibit more complex geometries than straight channels, mesh independence is further verified using a representative rectangular cavity (No. 5). The results in Table 2 confirm that the fourth mesh level also provides sufficient accuracy in this case. Therefore, this mesh configuration is consistently employed throughout the present study.

Table 2: Mesh independence of the microchannel with rectangular cavities.

No.	Grid Numbers ($\times 10^5$)	ΔP (kPa)	*e%*
1	3.6	39.06	3.06
2	8.6	39.74	1.38
3	14.5	39.95	0.86
4	48.9	40.21	0.21
5	98.3	40.29	–

2.4 Experimental Setup

The schematic of the micro-particle image velocimetry (Micro-PIV) system is presented in Fig. 2. The working fluid, polyethylene oxide (PEO), was seeded with fluorescent tracer particles (Thermo Fisher R0100)

at a mass ratio of 25:1. The particles had a diameter of 1 μm and a density of 1050 kg/m^3. A double-pulse neodymium-doped yttrium aluminum garnet (Nd:YAG) laser (532 nm) was employed to excite fluorescence at 610 nm, which was subsequently filtered by a dichroic lens and recorded by a charge-coupled device (CCD) camera. Velocity fields within the microchannel were obtained using an adaptive PIV algorithm implemented in Dynamic Studio. The differential pressure across the channel was measured using a high-precision differential pressure transducer (Rosemount 3051S) in conjunction with a data acquisition system (ADAM 4620) (Fig. 3). Both Newtonian and non-Newtonian fluids were injected to the channel inlet via a syringe pump (Harvard Apparatus). Both experimental variables (Δp and Q_v) are measured in dimensional units and processed using SI-consistent conversions. Dimensionless quantities (Re, f, Po, and f/f_0) are computed only in post-processing using the same definitions as the CFD model, ensuring experimental–numerical comparisons at matched nondimensional conditions rather than only matched flow rates.

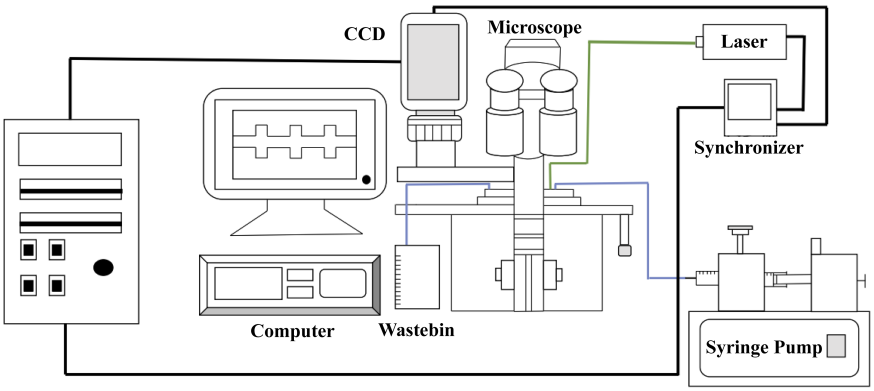

Figure 2: Schematic of micro-PIV system.

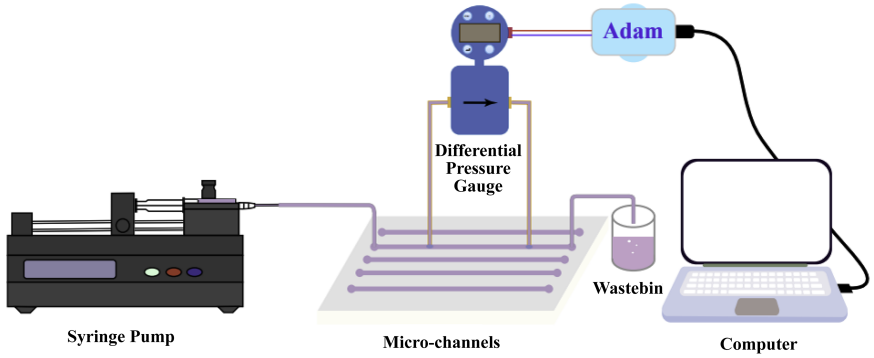

Figure 3: Schematic of the pressure monitoring system.

The uncertainty analysis of the experimental results is explored according to the standard error analysis method. According to the manufacturer specifications, the syringe pump (Harvard Apparatus) has a volumetric flow rate control accuracy of 0.25% and the differential pressure transducer (Rosemount 3051S) has a detection accuracy of 0.05%. Hence, the relative uncertainty of Re is calculated as follows:

$$\frac{\delta(Re)}{Re} = \sqrt{\left((2-\mathrm{n})\frac{\delta(u_{ave})}{u_{ave}}\right)^2} \tag{13}$$

The relative uncertainty of f is calculated as follows:

$$\frac{\delta(f)}{f} = \sqrt{\left(\frac{\delta(\Delta P)}{\Delta P}\right)^2 + \left(2\frac{\delta(u_{ave})}{u_{ave}}\right)^2} \tag{14}$$

The relative uncertainty of Po is calculated as follows:

$$\frac{\delta(Po)}{Po} = \sqrt{\left(\frac{\delta(\Delta P)}{\Delta P}\right)^2 + \left(\mathrm{n}\frac{\delta(u_{ave})}{u_{ave}}\right)^2} \tag{15}$$

For n = 0.79, the uncertainties of the Re, f, and Po are 0.3025%, 0.5025%, and 0.2037%, respectively. These uncertainty levels are very small, which confirms that the experimental data are reliable.

2.5 Model Validation

To ensure the reliability of the numerical model, the simulation results were validated against experimental measurements. Fig. 4 presents the flow field obtained from micro-PIV. As expected, the velocity near the channel wall and at the sharp corner of the cavity approaches zero, owing to the no-slip boundary condition and the formation of a stagnant vortex. Compared with Newtonian fluids, non-Newtonian fluids exhibit a more uniform velocity distribution across the cross-section. The obvious shear-thinning behavior that reduces fluid viscosity and the local shear stress. In contrast, Newtonian fluids generate larger velocity gradients, resulting in higher shear stresses and greater flow resistance. For non-Newtonian fluids, regions of low shear stress are observed at both flow rates (Q_v = 500 μL/h and Q_v = 10,000 μL/h). This indicates that Newtonian fluids consistently exhibit higher flow resistance, driven by stronger shear effects.

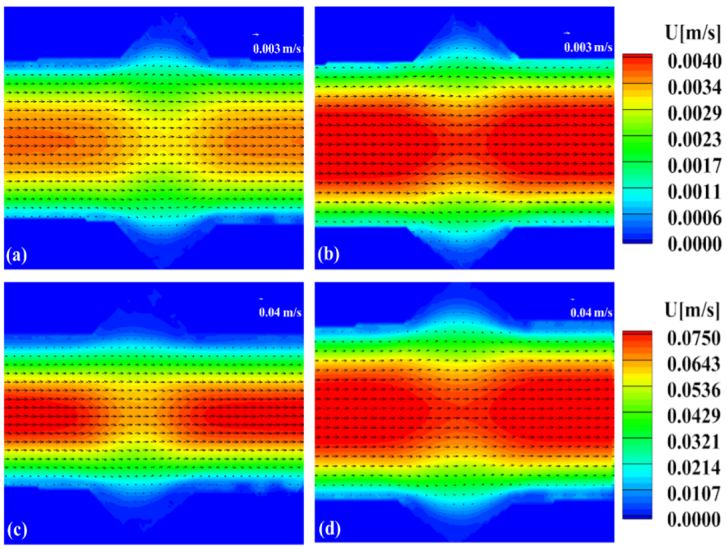

Figure 4: Velocity contours for the microchannel with isosceles triangular cavities. Non-Newtonian fluids (n = 0.79) for (**a**) Q_v = 500 μL/h and (**b**) Q_v = 10,000 μL/h. Newtonian fluids (n = 1) for (**c**) Q_v = 500 μL/h and (**d**) Q_v = 10,000 μL/h.

Fig. 5 presents the low shear force area of non-Newtonian fluid inside the cavity increases with the increase of flow velocity, indicating that vortices are formed inside the cavity at high flow velocities. In addition, it also confirms that the flow resistance of Newtonian fluid is greater than that of non-Newtonian fluid at different flow rates. This is because the channel inlet is a boundary condition with constant flow

rate, and the pressure resistance is generated by balancing the fluid shear force, so the pressure resistance of Newtonian fluid is greater.

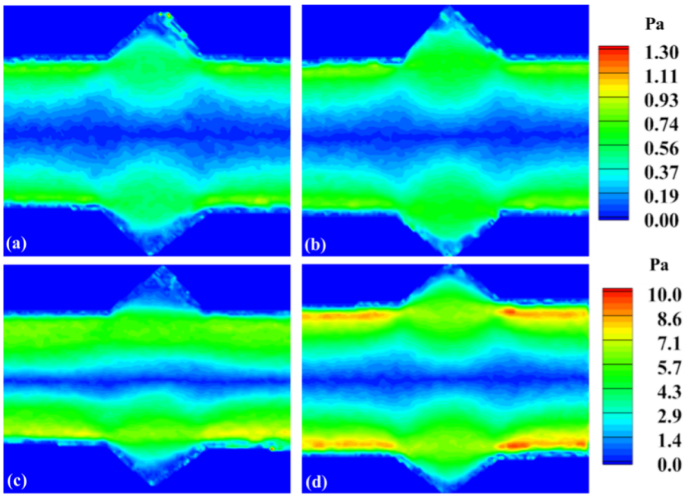

Figure 5: Shear stress contours for the microchannel with isosceles triangular cavities. Non-Newtonian fluids (n = 0.79) for (**a**) Q_v = 500 μL/h and (**b**) Q_v = 10,000 μL/h. Newtonian fluids (n = 1) for (**c**) Q_v = 500 μL/h and (**d**) Q_v = 10,000 μL/h.

Fig. 6 compares friction factor (f) of experimental and numerical results for the same microchannel geometry and operating conditions. Agreement of experimental data and numerical predictions verifies the accuracy of our numerical model. Notably, the microchannels with isosceles triangular cavities produce a clear drag-reduction effect compared with a smooth straight channel, as reflected in the decreasing friction factor f with increasing flow rate.

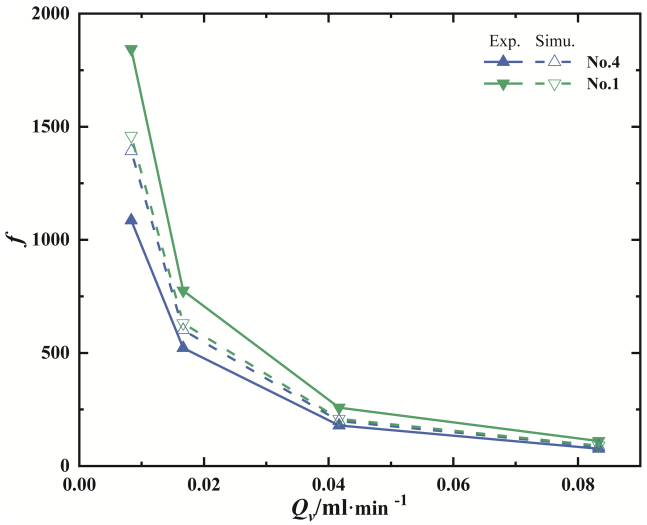

Figure 6: Comparison between experimental and numerical results.

3 Results and Discussion

3.1 Influence of Incidence Angle

Fig. 7a presents the variation of *Po* with flow rate for Newtonian and non-Newtonian fluids in a smooth straight channel. For the Newtonian case, *Po* remains essentially constant across the whole range. In contrast, the non-Newtonian fluid exhibits a pronounced increase in *Po* with flow rates with a non-linear growth trend.

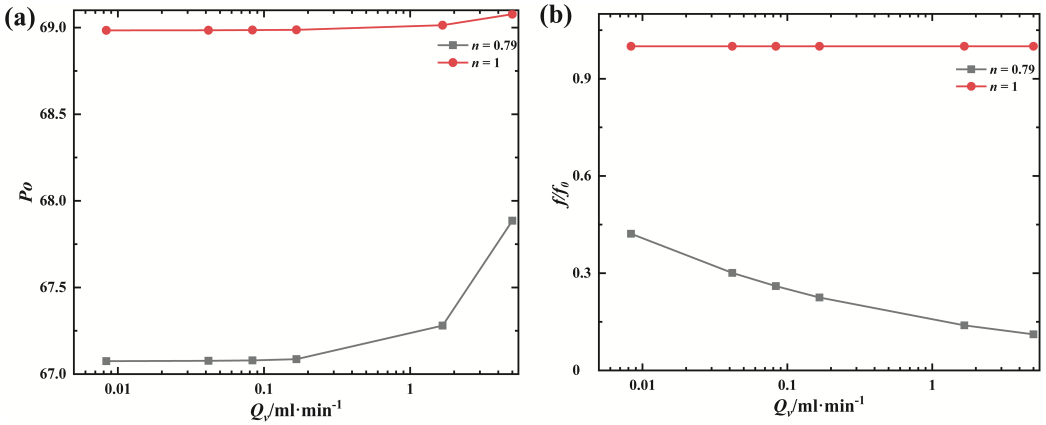

Figure 7: Variation of *Po* (**a**) and f/f_0 (**b**) with flow rates in the smooth straight microchannel.

As shown in Fig. 7b, the non-Newtonian fluids show superior drag-reduction performance. At a low flow rate of 0.01 mL/min, the drag reduction rate reaches 58%, and it increases almost linearly with flow rate, attaining 88.87% at 5 mL/min. This enhancement arises from shear-thinning effects: the effective viscosity of the fluid decreases as shear rate increases. The viscous stress is reduced and leads to the lower flow resistance.

To investigate the influence of cavity incidence angle on flow performance, numerical simulations were conducted for microchannels with left triangular cavities (No. 2), isosceles triangular cavities (No. 3), and right triangular cavities (No. 4), as illustrated in Fig. 8. At low flow rates, both Newtonian and non-Newtonian fluids exhibit nearly constant *Po*. Microchannels with cavities indicates lower flow resistance relative to the straight case, with No. 3 providing the greatest reduction, while No. 2 and No. 4 show similar behavior. For Newtonian fluids, the pressure drop in No. 3 is reduced by 5.8% compared with No. 1, whereas the reductions observed in No. 2 and No. 4 are both 5.3%. Among the non-Newtonian cases, No. 3 yields the largest pressure-drop reduction at 4.6% compared with No. 1, whereas No. 2 and No. 4 each show a slightly smaller but similar reduction of 4.3%. Therefore, No. 3 of non-Newtonian fluids exhibits the minimum flow resistance, achieving a maximum drag reduction of 7.3% compared with No. 1 using a Newtonian fluid. In this regime, non-Newtonian fluids maintain consistently lower *Po* than Newtonian fluids, highlighting that the combination of shear-thinning rheology and micro cavities enhances the drag reduction rate. At higher flow rates, *Po* rises especially for non-Newtonian fluids, whose flow resistance eventually surpasses that of Newtonian fluids. Consequently, No. 3 with Newtonian fluid yields the lowest flow resistance, with a 5.5% reduction relative to No. 1. This shift suggests the beneficial effect of shear thinning rheology is partially offset by micro cavities. Overall, No. 3 consistently exhibits the minimum resistance for both Newtonian and non-Newtonian fluids across all the flow conditions.

Figs. 9 and 10 show the pressure contours that clarify the mechanism of vortex formation. The sudden channel expansion produces a sharp local pressure drop and a reverse pressure gradient, which together drive recirculating flow inside the cavity. These cavities act as liquid–liquid interfaces that primarily reduce near-wall shear stress and leads to the drag reduction effect. Compared with Newtonian fluids, non-Newtonian

fluids exhibit a stronger tendency to form larger primary vortices along with secondary recirculation zones. At higher flow rates, vortices increasingly dominate within the cavities. Although micro cavities continue to decrease wall shear stress in both fluid types. Non-Newtonian fluids shows a higher viscosity relative to the straight channel due to their shear-thinning rheology, which reduces the corresponding drag-reduction effect. Consequently, the interaction between cavity vortices and shear thinning promotes drag reduction at low flow rates. However, this advantage is reduced at higher flow rates, leading to diminished overall performance. Poiseuille number (*Po*) compactly quantifies hydraulic resistance. At fixed flow rate, reduced *Po* corresponds to reduced pumping power ($P_{\text{pump}} = \Delta pQ$). In cavitied channels, changes in *Po* reflect a balance between reduced viscous losses (via shear redistribution and, for $n < 1$, lower apparent viscosity in high-shear regions) and added form losses associated with separation/reattachment and pressure recovery around cavity edges.

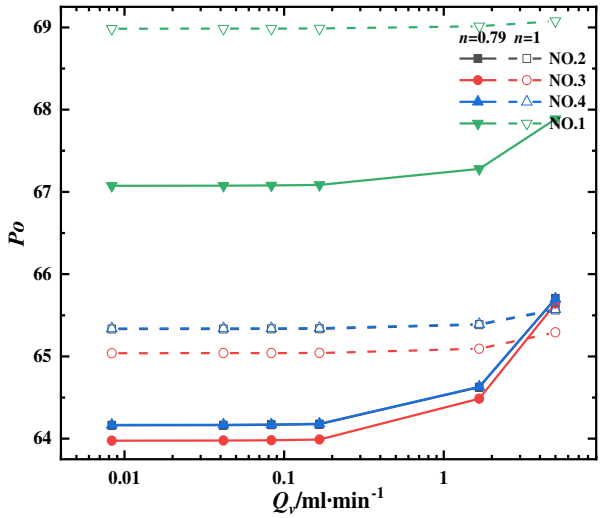

Figure 8: Variation of *Po* with flow rates at different incidence angles.

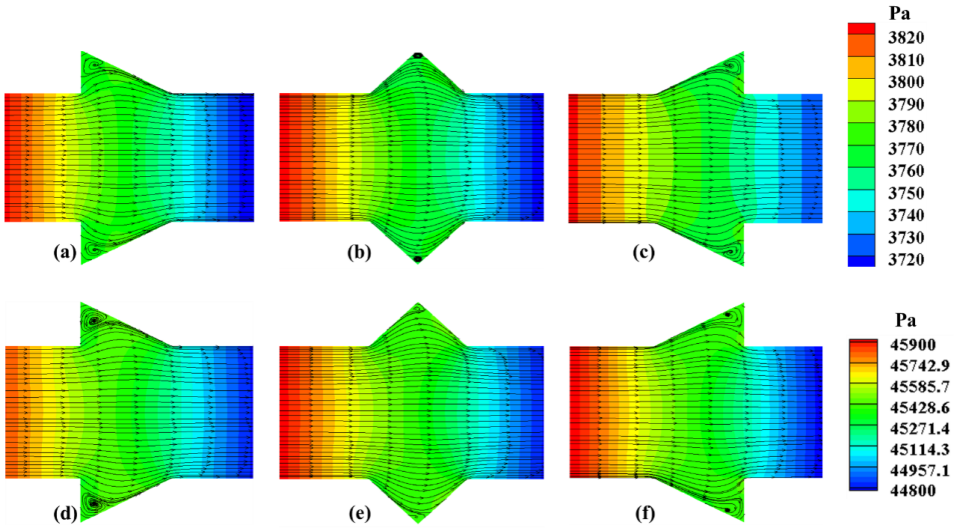

Figure 9: Pressure contours of Newtonian fluids in No. 2, No. 3 and No. 4: (**a**–**c**) for Q_v = 2400 μL/h; (**d**–**f**) for Q_v = 300,000 μL/h.

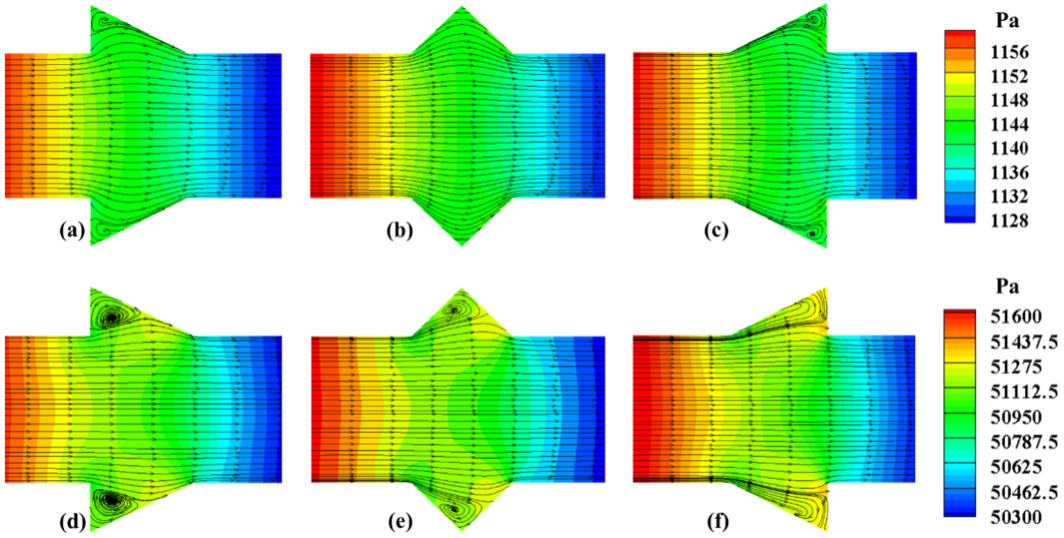

Figure 10: Pressure contours of non-Newtonian fluids in No. 2, No. 3 and No. 4: (**a**–**c**) for Q_v = 2400 μL/h; (**d**–**f**) for Q_v = 300,000 μL/h.

3.2 Influence of Structural Smoothness

The influence of structural smoothness on flow resistance is systematically evaluated for three microchannel configurations: rectangular (No. 5), trapezoidal (No. 6), and semicircular (No. 7). Across all designs, at low flow rates, the synergistic effect of shear-thinning rheology and cavity-induced vortices enhanced drag reduction, consistent with previously observed trends (Fig. 11). The maximum drag reduction rate is 7.6% for semicircular using non-Newtonian fluids in relative to No. 1 with Newtonian fluids. As the flow rate increased, however, the advantageous impact of shear-thinning behavior is partially counteracted by the micro cavities, leading to a diminished overall drag-reduction effect. The maximum drag reduction rate is 6.3% for semicircular using Newtonian fluids in relative to No. 1 with Newtonian fluids. Among the three structures, the semicircular cavity (No. 7), characterized by the highest degree of structural smoothness, consistently exhibited the lowest flow resistance. Analysis of streamline and pressure contours revealed that the smooth curvature of semicircular minimized flow separation and mitigated the formation of sharp recirculation zones, thereby reducing near-wall shear stress more effectively than No. 5 and No. 6 (Figs. 12 and 13). Overall, the results indicate that increased structural smoothness not only lowers flow resistance under a broad range of operating conditions but also moderates the interplay between shear-thinning rheology and microcavity, highlighting the importance of geometric design for optimized microfluidic performance.

Across cavity geometries, drag reduction reflects a balance between reduced viscous losses (via shear redistribution and, for $n < 1$, lower apparent viscosity in high-shear regions) and increased form losses associated with separation/reattachment and pressure recovery. Incidence angle and edge smoothness modify recirculation size and reattachment length, which is consistent with the pressure-contour gradients and Po trends reported in Figs. 8–13.

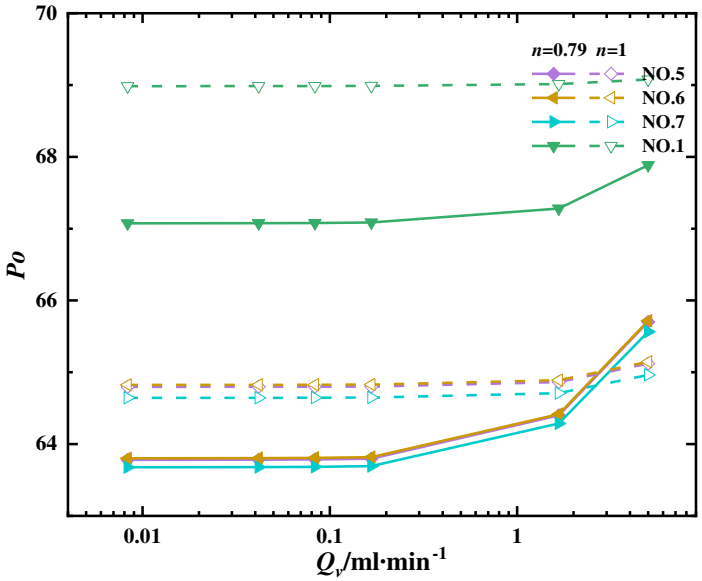

Figure 11: *Po* number vs. flow rate for different streamline degrees.

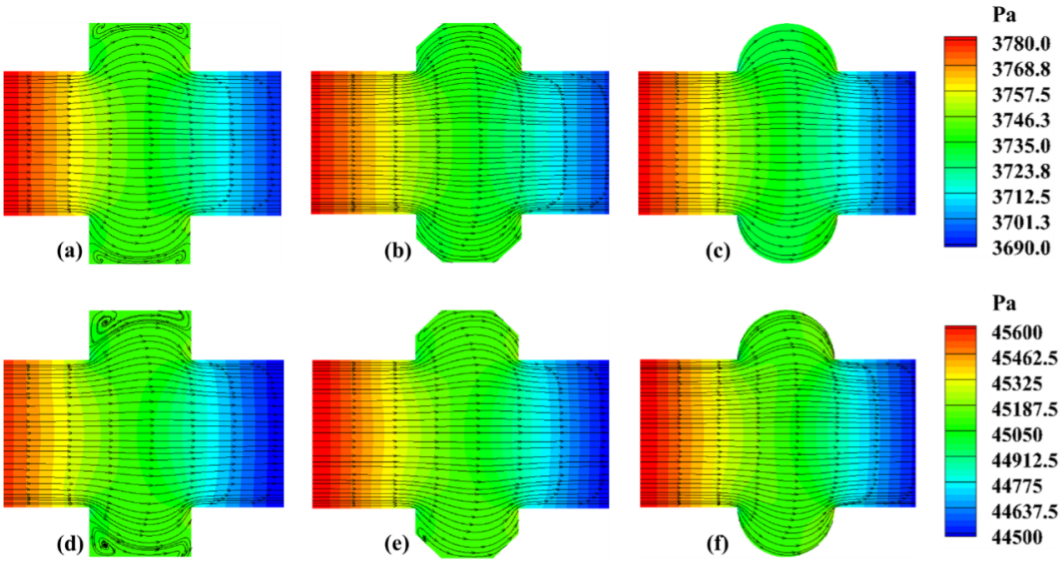

Figure 12: Pressure contours of Newtonian fluids in No. 5, No. 6 and No. 7: (**a**–**c**) for Q_v = 2400 μL/h; (**d**–**f**) for Q_v = 300,000 μL/h.

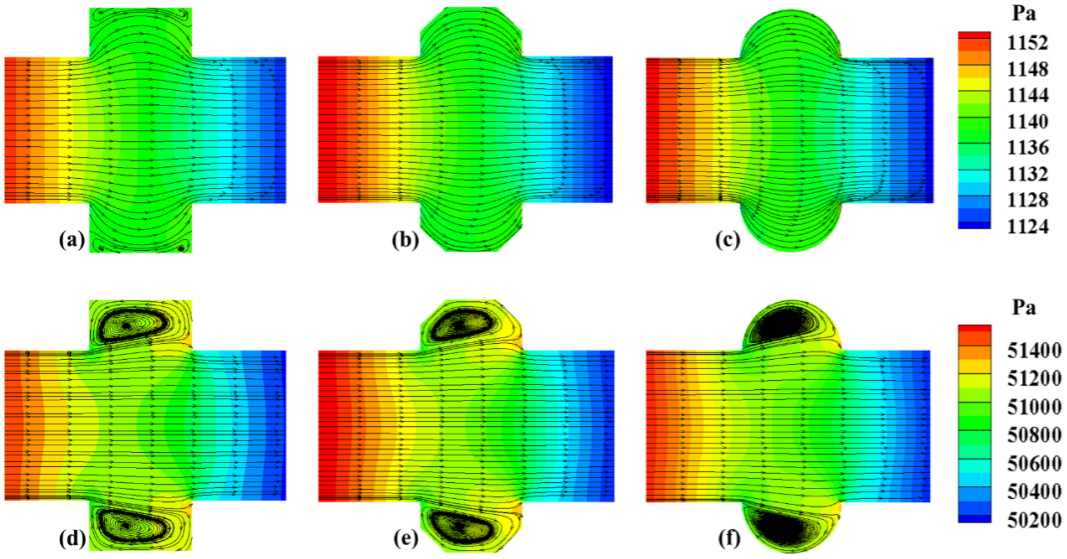

Figure 13: Pressure contours of non-Newtonian fluids in No. 5, No. 6 and No. 7: (**a**–**c**) for Q_v = 2400 μL/h; (**d**–**f**) for Q_v = 300,000 μL/h.

3.3 Influence of Non-Newtonian Characteristics

To systematically investigate the influence of non-Newtonian fluid parameters on flow resistance, we analyzed the effects of the zero-shear viscosity m and the power law index n in the semicircular microchannel at an average velocity of Q_v = 150,000 μL/h. As shown in Fig. 14, the increasing m leads to higher pressure drop with a nonlinear relationship. Specifically, when m increases from 0.003 to 0.03, the pressure drop increases by a factor of 8.58 due to the shearing thinning behavior. When m increases from 0.3 to 0.9, the pressure drop increases by a factor of 3, which is similar to Newtonian Fluids. Comparison with Newtonian fluids of same initial viscosity shows that non-Newtonian fluids consistently exhibit lower pressure drop, with the difference amplifying as m increases. For m = 0.9, the Newtonian pressure drop is 42 times higher than that of the corresponding non-Newtonian fluid.

The influence of non-Newtonian fluid properties on flow resistance is evaluated in the semicircular microchannel at Q_v = 150,000 μL/h, focusing on zero-shear viscosity (m) and flow behavior index (n). Fig. 14 shows that the pressure drop increases nonlinearly with m. A sharp rise is observed when m grows from 0.003 to 0.03, with an 8.58-fold increase due to shear-thinning effects. As m increases from 0.3 to 0.9, the pressure drop rises approximately threefold, similar to Newtonian scaling. Compared to Newtonian fluids of equal initial viscosity, non-Newtonian fluids consistently exhibit lower pressure drops. Generally, when m ranges from 0.003 to 0.9, the pressure drop of Newtonian fluids is 42 times greater than that of non-Newtonian fluids.

Similarly, the influence of the flow behavior index n was examined in the semicircular microchannel at m = 0.03 and Q_v = 150,000 μL/h. As shown in Fig. 15, the pressure drop increases exponentially with n, as larger n values diminish shear-thinning effects and approach Newtonian behavior. A small increment of 0.1 in n (from 0.9 to 1.0) produces nearly a 2.5-fold rise in pressure drop, underscoring the strong sensitivity of flow resistance to n. These findings confirm that both m and n critically shape the nonlinear pressure-drop response of non-Newtonian fluids.

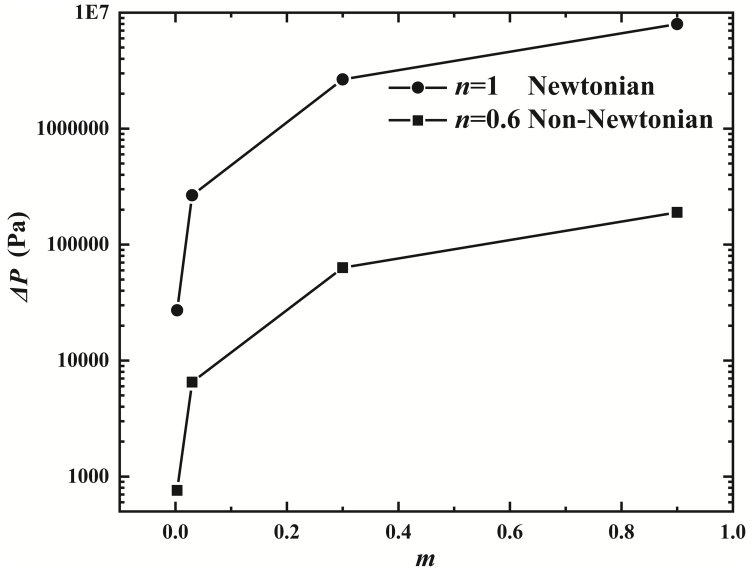

Figure 14: Effect of zero-shear viscosity m on pressure drop for n = 1 and 0.6.

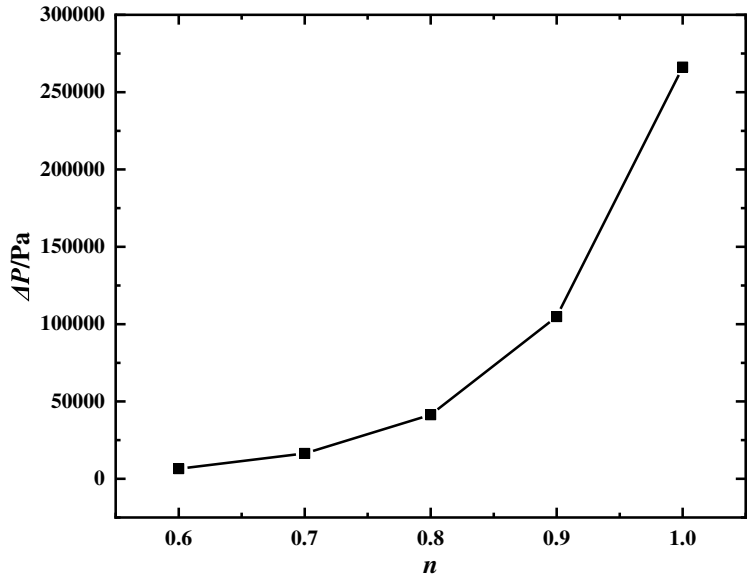

Figure 15: Effect of flow characteristic index n on pressure drop for m = 0.03.

3.4 Optimization of Shape Parameters

Given that the semicircular cavity exhibits the most pronounced drag reduction among the six geometries, this section adopts a controlled variable approach to introduce dimensionless parameters and systematically investigate the effects of aspect ratio (α), depth ratio (β), and spacing ratio (γ) on flow resistance. Table 3 demonstrates specific shape parameters that were investigated.

$$\alpha = \frac{L_c}{H_c} \tag{16}$$

$$\beta = \frac{W_c}{W} \tag{17}$$

$$\gamma = \frac{S}{L_c} \tag{18}$$

Table 3: Shape parameters.

Parameter	Value
α	2, 4, 8, 10
L_c/mm	0.2, 0.4, 0.8, 1
β	1.67, 2, 2.33, 3
H_c/mm	0.1, 0.15, 0.2, 0.3
γ	3, 5, 10, 15, 30, 75, 150
S/mm	64, 39, 20, 13, 7, 4, 2

The influence of aspect ratio α is illustrated in Fig. 16. In this analysis, the spacing ratio (γ = 5) and depth ratio (β = 1.67) are fixed, while the cavity depth is varied from 1.67 to 3. As Fig. 16a shows, *Po* decreases with increasing α, while the decreasing rate gradually diminishes, suggesting a marginal effect. At low flow rates (Q_v < 0.167 mL/min), *Po* remains essentially constant, indicating that viscous effects dominate with similar flow structures. However, once Q_v exceeds 0.167 mL/min, *Po* begins to increase with flow rate, reflecting the growing contribution of inertial effects. Fig. 16b presents the variation of the drag reduction ratio (f/f_0) with Q_v. The drag reduction effect is enhanced with the increasing flow rate, as indicated by the higher f/f_0 values. This trend stems from stronger shear-thinning at higher flow rates: elevated shear reduces the fluid viscosity near the walls, diminishes wall shear stress, and consequently lowers frictional losses.

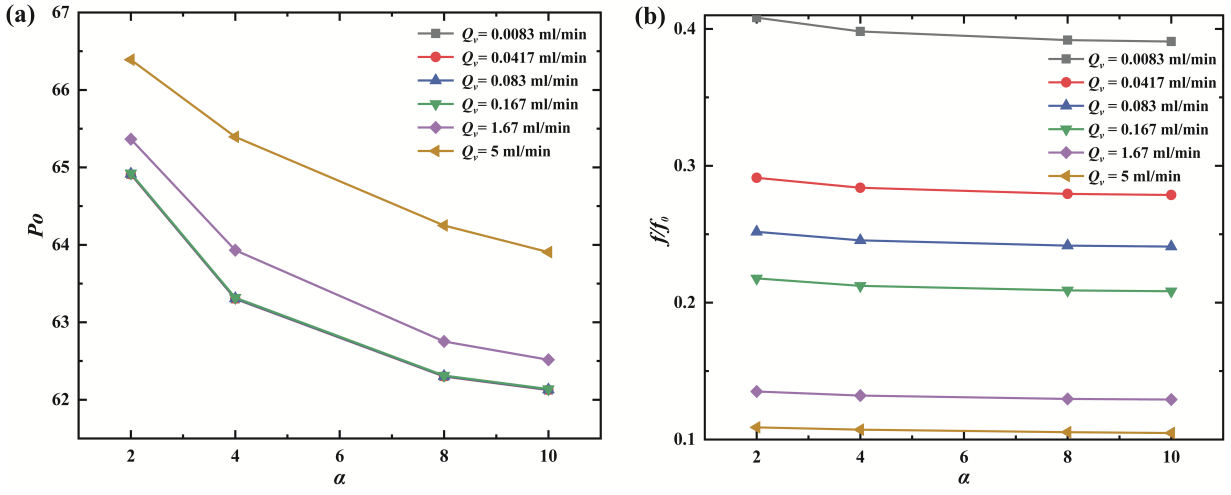

Figure 16: Effect of α on *Po* (**a**) and f/f_0 (**b**).

The influence of depth ratio β is illustrated in Fig. 17. In this analysis, the spacing ratio (γ = 4) and aspect ratio (α = 2) are fixed, while the cavity depth is varied from 1.67 to 3. The results from Fig. 17a indicate that *Po* remains nearly unchanged with increasing β. Fig. 17b illustrates that the drag reduction ratio (f/f_0) shows little sensitivity to β across different flow rates. This phenomenon can be attributed to the fact that excessively

deep cavities predominantly form stagnant zones within the cavity, thereby exerting minimal influence on the mainstream flow and contributing little to additional drag reduction.

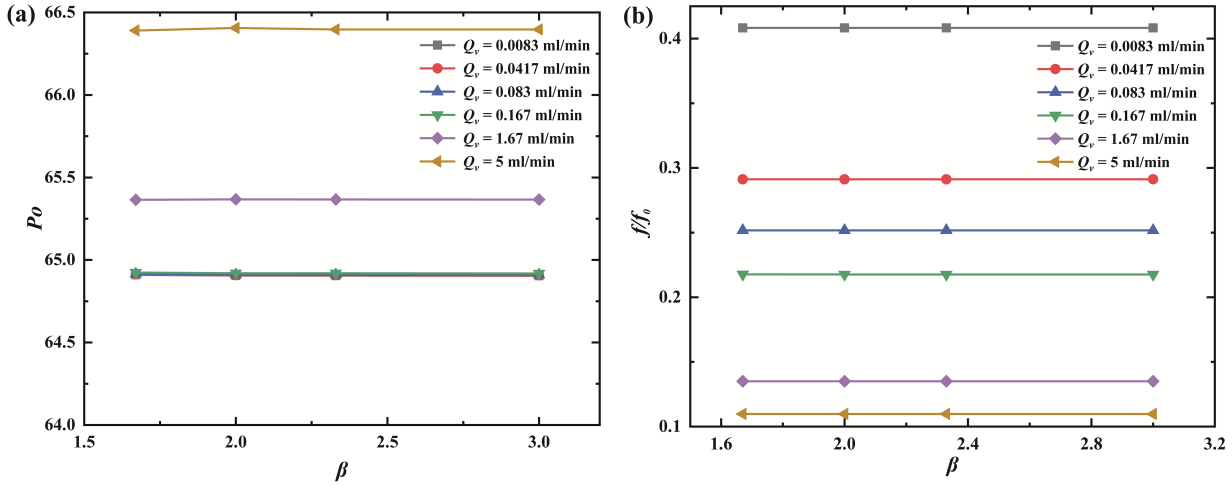

Figure 17: Effect of β on Po (**a**) and f/f_0 (**b**).

The influence of the spacing ratio (γ) on drag reduction was investigated at a fixed aspect ratio (α = 2) and depth ratio (β = 0.67). Fig. 18a indicates that Po rises with increasing β until flatten out. From Fig. 18b, the friction factor ratio (f/f_0) rises with γ in the range $3 \leq \gamma \leq 15$ and then remains nearly constant. This trend arises as the narrow spacing cause the vortices generated within adjacent cavities strongly interact with each other, reducing vortex stability and weakening drag reduction. As γ increases, these interactions diminish, strengthening the effective liquid–liquid interface created by the vortices and enhancing drag reduction. Once the spacing exceeds a critical value ($\gamma \geq 15$), the cavities are sufficiently isolated, and further increases in γ no longer contribute to additional drag reduction performance.

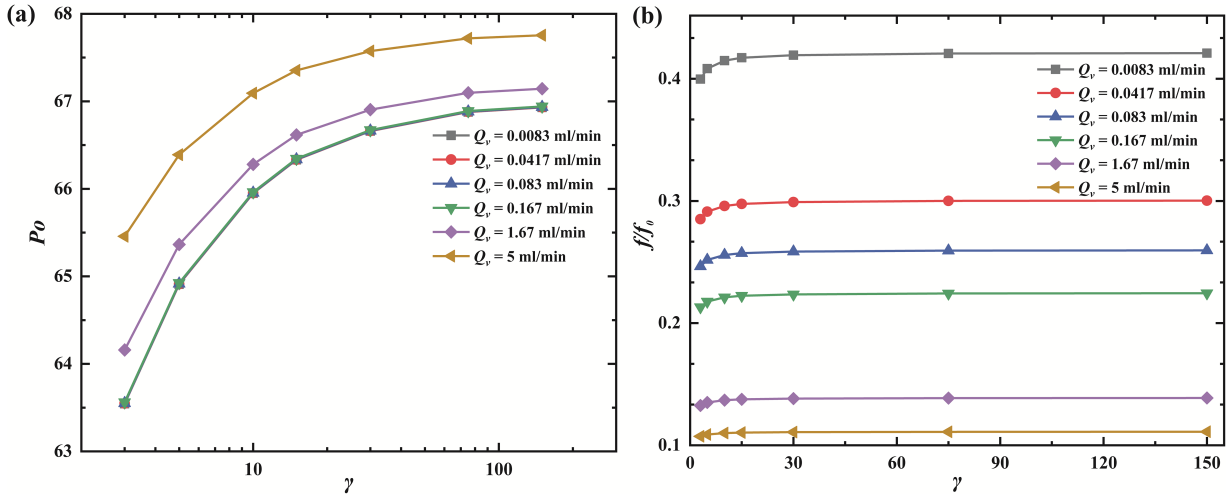

Figure 18: Effect of γ on Po (**a**) and f/f_0 (**b**).

4 Conclusions

In this study, the flow performance of non-Newtonian fluids in microchannels with different cavity structures was systematically investigated through a combination of numerical simulation and experimental measurements. The effects of cavity incidence angle, structural smoothness, non-Newtonian rheological parameters, and shape parameters were comprehensively analyzed. The major conclusions can be summarized as follows:

(1) Both cavities and non-Newtonian fluids contribute to drag reduction. Under low flow conditions, the combined effects achieve a peak drag reduction of 7.6% for semicircular with non-Newtonian fluids. At higher flow rates, their interplay reduces the overall benefit. Newtonian fluids achieve a maximum reduction of 6.3% for semicircular at a flow rate of 5 mL/min.

(2) Regarding the incidence angle, the isosceles triangular configuration exhibits the most pronounced drag reduction of 7.3%, comparing to 6.8% of left triangle and right triangle. The structural smoothness analysis indicates that semicircular cavities provide the best drag reduction rate of 7.6%, comparing to 7.4% of rectangle and trapezoid.

(3) For non-Newtonian parameters, both the zero-shear viscosity (m) and flow behavior index (n) exhibit nonlinear influences on the pressure drop. With n = 0.6, the pressure drop increases 8.58 times and 3 times when m increases from 0.003 to 0.3 and 0.3 to 0.9 respectively. With m = 0.03, a 0.1 increment of n results a 2.5 times increase of pressure drop. Specifically, increasing m results in higher flow resistance but with a progressively weakening effect, while increasing n increases the pressure drop but with an amplifying influence.

(4) In terms of shape parameters, the aspect ratio (α), depth ratio (β), and spacing ratio (γ) all demonstrate marginal effects. Within the scope of the present study, the depth ratio (β) has negligible influence on the drag reduction effect. *Po* remains nearly independent with the flow rate when $Q_v < 0.167$ mL/min, whereas for $Q_v > 0.167$ mL/min, *Po* gradually increases with the flow rate. When α increases from 2 to 10, the decrease rate of *Po* increases with flow rate, with and average decrease rate of 4%. The friction factor ratio (f/f_0) rises with γ in the range $3 \leq \gamma \leq 15$ and then remains nearly constant.

Overall, this work highlights that the interplay between fluid rheology and micro cavities governs the drag reduction mechanism. The findings provide fundamental insights for the design and optimization of microchannel structures to enhance flow efficiency of non-Newtonian fluids in energy-related applications.

Acknowledgement: Not applicable.

Funding Statement: This work is supported by the Stable Support Project (title: Characteristics and Design of Controllable Phase-Change Cooling in Micro/Nano-channels under High-Mach-Number Rotating Conditions, & ID: 12700002025146001) from National Key Laboratory of Science and Technology on Aero-Engine Aero-thermodynamics and National Natural Science Foundation of China (No. 52006005 and No. 12302362).

Author Contributions: Yi Huang: Writing—original draft, Investigation, Conceptualization. Ran Gao: Methodology, Formal analysis, Data curation. Hao Ye: Methodology, Investigation. Weidong Fang: Investigation. Xiaopeng Shang: Methodology, Formal analysis. Haiwang Li: Validation, Supervision, Project administration. All authors reviewed and approved the final version of the manuscript.

Availability of Data and Materials: The data supporting the findings of this study is available from the author, Dr. Yi Huang, upon reasonable request.

Ethics Approval: The article does not include human participants and/or animals research.

Conflicts of Interest: The authors declare no conflicts of interest.

Nomenclature

D_h	Hydraulic diameter
f	Drag coefficient
H_c	Cavity height
Kn	Knudsen number
L	Length of channel
L_c	Cavity width
m	Consistency coefficient
n	Power law index
Po	Poiseuille number
p	Pressure
p_{out}	Outlet pressure
Δp	Pressure dropt
Q_v	Volume flow rate
Re	Reynolds number
s	Cavity spacing
T_f	Fluid temperature
T_{in}	Inlet temperature
u	X direction velocity
u_{in}	Inlet velocity
v	Y direction velocity
W_c	Cavity width
w	Z direction velocity
x, y, z	Direction of x, y, z
Greek symbols	
α	Dimensionless parameters for cavity aspect ratio
β	Dimensionless parameters for cavity depth ratio
γ	Dimensionless parameters for cavity spacing ratio
$\dot{\gamma}$	Shear rate
θ	Angular displacement
μ	Kinematic viscosity
ρ	Fluid density
τ	Shear stress
Ω	Angular velocity

References

1. Song Y, Zhou Y, Zhang K, Fan Z, Zhang F, Wei M. Microfluidic programmable strategies for channels and flow. Lab Chip. 2024;24(19):4483–513. doi:10.1039/d4lc00423j.
2. Gholizadeh A, Mazzucchelli G, Gilet T. Flipping: a valve-free strategy to control fluid flow in centrifugal microfluidic systems. Sens Actuat B Chem. 2024;412(1):135778. doi:10.1016/j.snb.2024.135778.
3. Wibowo D, Zhao CX, He Y. Fluid properties and hydrodynamics of microfluidic systems. In: Santos HA, Liu D, Zhang H, editors. Microfluidics for pharmaceutical applications. Norwich, NY, USA: William Andrew Publishing; 2019. p. 37–77. doi:10.1016/b978-0-12-812659-2.00002-8.
4. Gurkan UA, Wood DK, Carranza D, Herbertson LH, Diamond SL, Du E, et al. Next generation microfluidics: fulfilling the promise of lab-on-a-chip technologies. Lab Chip. 2024;24(7):1867–74. doi:10.1039/d3lc00796k.

5. Kuang L, Zeng J, Boutelle M, Georgiou P. Live demonstration: a lab-on-chip platform for dynamic biosensing of fluids. In: Proceedings of the 2024 IEEE Biomedical Circuits and Systems Conference (BioCAS); 2024 Oct 24–26; Xi'an, China. doi:10.1109/biocas61083.2024.10798408.
6. Gao J, Hu Z, Yang Q, Liang X, Wu H. Fluid flow and heat transfer in microchannel heat sinks: modelling review and recent progress. Therm Sci Eng Prog. 2022;29(2):101203. doi:10.1016/j.tsep.2022.101203.
7. Coskun T, Cetkin E. A review of heat and fluid flow characteristics in microchannel heat sinks. Heat Trans. 2020;49(8):4109–33. doi:10.1002/htj.21819.
8. Weisbach J. Lehrbuch der ingenieur-und maschinen-mechanik. Braunschweig, Germany: F. Vieweg und Sohn; 1850. (In German).
9. George KE. Non-Newtonian fluid mechanics and polymer rheology. In: Thomas S, Weimin Y, editors. Advances in polymer processing. Cambridge, UK: Woodhead Publishing; 2009. p. 13–46. doi:10.1533/9781845696429.1.13.
10. Prasad V. Rheology of Non-Newtonian slurries and its effects on pipeline transportation for economical handling of bulk iron ore. Chem Eng Res Des. 2025;217(2):304–17. doi:10.1016/j.cherd.2025.04.012.
11. Lynch S, Nama N, Figueroa CA. Effects of non-Newtonian viscosity on arterial and venous flow and transport. Sci Rep. 2022;12(1):20568. doi:10.1038/s41598-022-19867-1.
12. Pal R. Non-Newtonian behaviour of suspensions and emulsions: review of different mechanisms. Adv Colloid Interface Sci. 2024;333(77):103299. doi:10.1016/j.cis.2024.103299.
13. Chakraborty S. Non-Newtonian fluids in microchannel. In: Li D, editor. Encyclopedia of microfluidics and nanofluidics. New York, NY, USA: Springer New York; 2015. p. 2427–40. doi:10.1007/978-1-4614-5491-5_1128.
14. Varshegaa S, Ragulkumar E, Peter F, Loganathan K, Sambath P. Thermal and mass transfer performance of non-Newtonian fluids under MHD and chemical reaction effects with thermophoresis and Brownian motion. Discov Appl Sci. 2025;7(7):748. doi:10.1007/s42452-025-07369-4.
15. Ren Q, Wang Y, Lin X, Chan CL. AC electrokinetic induced non-Newtonian electrothermal blood flow in 3D microfluidic biosensor with ring electrodes for point-of-care diagnostics. J Appl Phys. 2019;126(8):084501. doi:10.1063/1.5099272.
16. Yaghoubzadeh Vishkaei M, Javaherdeh K. Evaluating the efficiency and effectiveness of non-Newtonian fluid flow in a double-pipe heat exchanger with porous medium via numerical simulation. Numer Heat Transf Part A Appl. 2025;86(15):5431–52. doi:10.1080/10407782.2024.2330087.
17. Bayareh M. An overview of non-Newtonian nanofluid flow in macro- and micro-channels using two-phase schemes. Eng Anal Bound Elem. 2023;148(5):165–75. doi:10.1016/j.enganabound.2022.12.033.
18. Chhabra RP. Non-Newtonian fluids: an introduction. In: Krishnan JM, Deshpande AP, Kumar PBS, editors. Rheology of complex fluids. New York, NY, USA: Springer; 2010. p. 3–34. doi:10.1007/978-1-4419-6494-6_1.
19. Chen L, Yang Y, Song X, Zhang X, Gong Y, Peng C. Study on the influence of non-Newtonian fluid characteristics on the hydraulic performance and internal flow field of multiphase pump. Chem Eng Res Des. 2024;202:178–90. doi:10.1016/j.cherd.2023.12.022.
20. Fischer N, Masoudian M, Germann N. Impact of non-Newtonian fluid behavior on hydrodynamics and mass transfer in spacer-filled channels. Fluid Dyn Res. 2020;52(6):065502. doi:10.1088/1873-7005/abb91e.
21. Tang GH, Lu YB, Zhang SX, Wang FF, Tao WQ. Experimental investigation of non-Newtonian liquid flow in microchannels. J Non Newton Fluid Mech. 2012;173–174:21–9. doi:10.1016/j.jnnfm.2012.02.001.
22. Dong X, Liu X. Multi-objective optimization of heat transfer in microchannel for non-Newtonian fluid. Chem Eng J. 2021;412:128594. doi:10.1016/j.cej.2021.128594.
23. Chen SJ, Li S, Hu ZZ. Fluid flow and heat transfer characteristics of manifold microchannel heat sinks with ribs of different shapes. Int J Heat Mass Transf. 2025;251(4):127300. doi:10.1016/j.ijheatmasstransfer.2025.127300.
24. Huang B, Li H, Xia S, Xu T. Experimental investigation of the flow and heat transfer performance in micro-channel heat exchangers with cavities. Int J Heat Mass Transf. 2020;159(9):120075. doi:10.1016/j.ijheatmasstransfer.2020.120075.
25. Gräfner SJ, Wu PY, Kao CR. Flow in a microchannel filled with arrays of numerous pillars. Int J Heat Fluid Flow. 2022;97(1):109045. doi:10.1016/j.ijheatfluidflow.2022.109045.

26. Li P, Zhang D, Xie Y, Xie G. Flow structure and heat transfer of non-Newtonian fluids in microchannel heat sinks with dimples and protrusions. Appl Therm Eng. 2016;94:50–8. doi:10.1016/j.applthermaleng.2015.10.119.
27. Raihan MK, Jagdale PP, Wu S, Shao X, Bostwick JB, Pan X, et al. Flow of non-Newtonian fluids in a single-cavity microchannel. Micromachines. 2021;12(7):836. doi:10.3390/mi12070836.
28. Farahani SD, Hosseni M, Zakinia A, Öztop HF. Control of non-Newtonian fluid flow and heat transfer in microchannel by using porous triangular ribs and pulsating jet. Eur Phys J Plus. 2022;137(6):737. doi:10.1140/epjp/s13360-022-02954-7.
29. Vajravelu K, Prasad KV, Datti PS, Raju BT. Convective flow, heat and mass transfer of Ostwald-de Waele fluid over a vertical stretching sheet. J King Saud Univ Eng Sci. 2017;29(1):57–67. doi:10.1016/j.jksues.2014.04.009.